

# Stripe formation in bacterial systems with density-suppressed motility

Xiongfei Fu,<sup>1</sup> Lei-Han Tang,<sup>2,3</sup> Chenli Liu,<sup>4</sup> Jian-Dong Huang,<sup>4</sup> Terence Hwa,<sup>5</sup> and Peter Lenz<sup>6</sup>

<sup>1</sup>*Department of Physics, The University of Hong Kong, Pokfulam, Hong Kong, China*

<sup>2</sup>*Department of Physics, Hong Kong Baptist University, Kowloon Tong, Kowloon, Hong Kong, China*

<sup>3</sup>*Beijing Computational Science Research Center, 3 Heqing Road, Haidian, Beijing 100084, China*

<sup>4</sup>*Department of Biochemistry, The University of Hong Kong, Pokfulam, Hong Kong, China*

<sup>5</sup>*Center for Theoretical Biological Physics, University of California at San Diego, La Jolla, CA, USA*

<sup>6</sup>*Department of Physics and Center for Synthetic Microbiology, University of Marburg, Marburg, Germany*

(Dated: October 16, 2018)

Engineered bacteria in which motility is reduced by local cell density generate periodic stripes of high and low density when spotted on agar plates. We study theoretically the origin and mechanism of this process in a kinetic model that includes growth and density-suppressed motility of the cells. The spreading of a region of immotile cells into an initially cell-free region is analyzed. From the calculated front profile we provide an analytic ansatz to determine the phase boundary between the stripe and the no-stripe phases. The influence of various parameters on the phase boundary is discussed.

PACS numbers: 87.18.Hf, 87.23.Cc

Biological systems exhibit a wide variety of exquisite spatial and temporal patterns. These patterns often play vital roles in embryogenesis and development [1, 2]. In addition, colonies of bacteria and simple eukaryotes also generate complex shapes and patterns [3–8]. Typically, these patterns are the outcome of coordinated cell growth, movement, and differentiation that involve the detection and processing of extracellular cues [3].

These experimental observations have triggered extensive mathematical modeling. A large body of theoretical work is devoted to pattern formation by chemotactic bacteria. On the mean-field level, these phenomena can be described by Keller-Segel type reaction-diffusion models [9–11]. In many instances, the models invoke non-linear diffusion of the cells where the diffusion coefficient increases with the local cell density [3, 12].

Recently, it was theoretically proposed that the opposite case of density suppressing motility could also lead to patterns via a “self-trapping” mechanism [13, 14]. In parallel, we have explored such a system experimentally, using a synthetic biology approach [15]. The density-suppressed motility was introduced into the bacterium *E. coli* by having it excrete a small (and rapidly degraded) signaling molecule AHL, such that at low AHL levels, these cells perform random walks via their swim-and-tumble motion [16] and are “motile”, while at high AHL levels, these cells tumble incessantly, resulting in a vanishing macroscopic motility and becoming “immotile” [Fig. 1(a)].

On agar plates, these engineered bacteria form highly regular and stable stripe patterns consisting of periodically alternating regions of high and low cellular densities [Fig. 1(b)]. A thorough characterization of these spatial patterns gave rise to the following key experimental observations [15]: (i) Regulation of cell motility by AHL is essential for pattern formation; (ii) Cells are motile at low densities and immotile at high densities; (iii) Bacteria

form stripes sequentially in one- and two-dimensional geometries when expanding into an initially cell-free region; (iv) Random initial conditions do not give rise to stripes; (v) Chemotaxis is not required for pattern formation; (vi) The stripe patterns depend on the magnitude of the un-repressed cellular motility in the low density limit: Upon decreasing this magnitude the system makes a transition from a phase with spatially periodic stripes (the stripe phase) to the no-stripe phase, through a region with a finite number of stripes.

As demonstrated in [15], all the experimental observations can be reproduced by a three-component model that (i) describes the cellular motion as random walk with an abrupt AHL-dependent motility coefficient, (ii) takes into account the synthesis, diffusion, and turnover of AHL, and (iii) implements the consumption and diffusion of the nutrient due to cell growth and the limitation of growth in the absence of nutrient.

Despite the success of this model, the origin and mech-

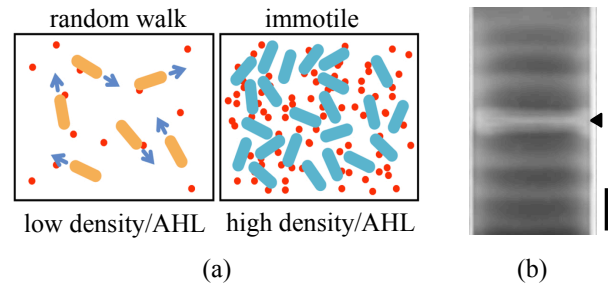


FIG. 1: (a) The engineered bacterium cells execute “random walks” at low densities but become immotile at high densities. (b) This coupling between density and motility leads to the formation of stripes with periodic density variations on agar plates [15]. Initial cell seeding was done (at the position indicated by the arrow) 30hr before the picture was taken. Bar corresponds to a length of 5mm.

anism of the pattern formation process remain unclear. In this paper, we describe a simplified two-component model to study the essential features of stripe formation analytically. In terms of the concentration  $h(x, t)$  of AHL and the cell density  $\rho(x, t)$  at position  $x$  and time  $t$ , the dynamical equations are given by,

$$\frac{\partial h}{\partial t} = D_h \frac{\partial^2 h}{\partial x^2} + \alpha \rho - \beta h, \quad (1)$$

$$\frac{\partial \rho}{\partial t} = \frac{\partial^2}{\partial x^2} [\mu(h) \rho] + \gamma \rho \left( 1 - \frac{\rho}{\rho_s} \right). \quad (2)$$

The first equation describes production (with rate  $\alpha$ ), diffusion (with diffusion coefficient  $D_h$ ) and turnover (with rate  $\beta$ ) of AHL. It is clear that in spatially homogeneous situations,  $h \propto \rho$  in the steady state, hence the name ‘‘quorum sensor’’ for AHL. The second term on the right hand side of Eq. (2) describes logistic bacterial growth at rate  $\gamma$  and with a saturation density  $\rho_s$ . The reduced growth rate at high densities approximates the nutrient depletion effect in the experiments. The stochastic swim-and-tumble motion of the bacteria is modeled as a diffusion-like term on the right hand side of Eq. (2). The experimentally measured values of all parameters can be found in Ref. [15].

The motility function  $\mu(h)$  explicitly depends on  $h$ . It takes into account the repressive effect of AHL concentration (and hence cell density) on cell motility. The interaction term in Eq. (2) can be obtained by either generalizing the coarse-graining procedure of Ref. [13] or adopting the master equation approach of Ref. [17] to an  $h$ -dependent motility. In fact, such an analysis yields a mixture of two terms  $\partial_x(\mu(h)\partial_x\rho)$  and  $\partial_x(\rho\partial_x\mu(h))$  (for details see SM). For simplicity we focus on the above coupling, but our main conclusions are not affected by this (for details see SM).

Measurements of bacterial diffusion at the population level show that  $\mu$  drops abruptly from a value  $D_\rho$  to  $D_{\rho,0} \ll D_\rho$  as  $h$  increases beyond a threshold  $h_0$ . As simulation results of Ref. [15] did not depend sensitively on the value  $D_{\rho,0}$ , we shall set  $D_{\rho,0} = 0$ . Thus, we consider the form  $\mu(h) = D_\rho$  for  $h \leq h_0 - w$  and  $\mu(h) = 0$  for  $h > h_0$  with a linear decrease of  $\mu$  for the transition region  $h_0 - w < h < h_0$  with  $h_0 \gg w \rightarrow 0$ .

As demonstrated in Ref. [15], this two-component model is able to initiate stripe patterns in a growing bacteria colony and maintain them for a while; but the stripes are eventually lost after long times when cell densities reach  $\rho_s$  throughout the system. The latter behavior deviates from the experimental system where stripes are frozen in upon nutrient exhaustion. Nevertheless, the model correctly captures the dynamics at the propagating front where new stripes are formed. The simplicity gained enables analytic treatment that clarifies conditions for spontaneous stripe formation in the system.

Consider a one-dimensional bacterial colony development as depicted in Fig. 1(b). Initially, cell density is

low on the plate and all cells grow and freely diffuse. As growth proceeds cells at the center aggregate. The increased cell population boosts the local AHL concentration, driving it eventually above  $h_0$  so that cells inside the aggregate become immotile. At the same time, this high density region expands outward by absorbing cells moving from surrounding low-density regions into the aggregate. Depending on the parameter values of the system, the high density region expands either stably as a front or exhibits instability that results in stripes [15].

We now take a closer look at the low-density region that precedes the advancing aggregate, whose cell density profile is calculated later (see Fig. 2). The size of this motile cell population is maintained by a dynamic balance between cell growth within and loss to the aggregate in the contact zone. Due to absorption by the aggregate, cell number is low in the contact region. By virtue of Eq. (2), the maximum density  $\rho_m$  of motile cells is found at a distance  $L_\rho = \sqrt{D_\rho/\gamma}$  from the aggregate, while the cell diffusion flux into the aggregate is given by  $J \simeq D_\rho \rho_m / L_\rho$ . Meanwhile, the expansion speed  $c$  of the aggregate satisfies  $J = c \rho_c$  where  $\rho_c$  is the density drop across the aggregate boundary. Hence quite generally  $\rho_m \simeq \rho_c$ , i.e., the cell density profile in the motile region scales with the density at the edge of the aggregate where the AHL concentration is at the threshold value  $h_0$ . A quantitative calculation is then required to determine whether the AHL concentration rises to the threshold again at  $\rho_m$ . As we shall see below, the answer depends on how the diffusion length  $L_h = \sqrt{D_h/\beta}$  of AHL molecules (i.e., the typical distance travelled by an AHL molecule before degradation) compares to  $L_\rho$ .

We will analyze a rescaled version of the model (1)-(2) that only depends on dimensionless quantities. We measure length in units of  $L_\rho$ , time in units of  $1/\gamma$ ,  $\rho$  in units of  $\beta h_0/\alpha$  and  $h$  in units of  $h_0$ . All dimensionless quantities are denoted by a hat (e.g.  $\hat{t} \equiv t\gamma$  etc.). For a steadily propagating front at speed  $\hat{c}$ , the density profiles  $\hat{\rho}$  and  $\hat{h}$  become functions of  $\hat{z} = \hat{x} - \hat{c}\hat{t}$ . We set the front position at  $\hat{z} = 0$  such that cells are immotile for  $\hat{z} < 0$  (region I) and motile for  $\hat{z} > 0$  (region II).

The cell density profile in region I is easily obtained by integrating Eq. (2) with the boundary condition  $\hat{\rho}_I(-\infty) = \hat{\rho}_s \equiv \alpha \rho_s / (\beta h_0)$ ,

$$\hat{\rho}_I(\hat{z}) = \frac{\hat{\rho}_s \hat{\rho}_c}{\hat{\rho}_c + (\hat{\rho}_s - \hat{\rho}_c) e^{\hat{z}/\hat{c}}}, \quad (3)$$

where  $\hat{\rho}_c \equiv \hat{\rho}_I(0^-)$  is the scaled cell density at the edge of the aggregate. The experimental system of Ref. [15] has a  $\hat{\rho}_s \simeq 4$ .

In region II, the marginal stability criterion [18] yields  $\hat{\rho}_{II}(\hat{z}) \sim e^{-\hat{z}}$  for  $\hat{z} \gg 1$  with the selected wave speed  $\hat{c} = 2$ . With this choice, Eq. (2) takes on the following form (except within a distance  $w$  from the interface),

$$\hat{\rho}_{II}'' + 2\hat{\rho}_{II}' + \hat{\rho}_{II}(1 - \hat{\rho}_{II}/\hat{\rho}_s) = 0, \quad (4)$$

where the prime denotes  $d/d\hat{z}$ . For the form of  $\mu(h)$  described, one finds  $\hat{\rho}_{\text{II}}(0^+) = 0$  as  $w \rightarrow 0$  (see SM). Matching the diffusional flux from the motile side with the speed of the immotile front yields the second condition at the interface:  $\hat{\rho}'_{\text{II}}(\hat{z} = 0^+) = 2\hat{\rho}_c$ . Thus,  $\hat{\rho}_{\text{II}}(\hat{z})$  is a non-monotonic function, rising for small  $\hat{z}$  before decaying exponentially for large  $\hat{z}$ .

The AHL profile is determined from the cell density profile as

$$\hat{h}(\hat{z}) = \hat{\beta} \int_{-\infty}^{\infty} d\hat{z}_1 \hat{\rho}(\hat{z}_1) G_h(\hat{z} - \hat{z}_1), \quad (5)$$

with the Green's function,

$$G_h(\hat{z}) = -(1 + \hat{D}_h \lambda) e^{-\hat{z}/\hat{D}_h} e^{(1 + \hat{D}_h \lambda)|\hat{z}|/\hat{D}_h} / 2, \quad (6)$$

and  $\lambda \equiv -[1 + (1 + \hat{D}_h \hat{\beta})^{1/2}] / \hat{D}_h$ .

Due to the nonlinearity in Eq. (4), an exact solution for  $\hat{\rho}_{\text{II}}$  is not possible and we shall analyze the problem in an expansion in  $\varepsilon \equiv \hat{\rho}_c / \hat{\rho}_s = \rho_c / \rho_s$ . We shall first consider the limit  $\varepsilon \rightarrow 0$ . The solution (3) is then approximated by  $\hat{\rho}_{\text{I}}(\hat{z}) \simeq \hat{\rho}_{\text{I}}^{\text{lin}}(\hat{z}) = \hat{\rho}_c e^{-\hat{z}/2}$ . The linear form of Eq. (4) together with the matching conditions at  $\hat{z} = 0$  yields  $\hat{\rho}_{\text{II}}^{\text{lin}}(\hat{z}) = 2\hat{\rho}_c \hat{z} e^{-\hat{z}}$ . Inserting  $\hat{\rho}_{\text{II}}^{\text{lin}}(\hat{z})$  into (5), we obtain the AHL profile to the zeroth order in  $\varepsilon$ ,

$$\hat{h}_{\text{II}}^{\text{lin}}(\hat{z}) = \hat{\beta} \hat{\rho}_c \left( \frac{4 - 4\hat{D}_h}{v^2} e^{-\hat{z}} + \frac{2}{v} \hat{z} e^{-\hat{z}} + \frac{\lambda^2}{w} e^{\lambda \hat{z}} \right), \quad (7)$$

with  $v \equiv 2 - \hat{D}_h + \hat{\beta}$  and  $w \equiv (1 + \lambda)^2 (1 + 2\lambda) (1 + \hat{D}_h \lambda)$ . The value of  $\hat{\rho}_c$  is determined by the definition of the front at  $\hat{z} = 0$ , i.e.  $\hat{h}_{\text{II}}^{\text{lin}}(0) = 1$ .

Higher order corrections to the analytical profiles given above can be computed systematically by rewriting Eq. (4) in the form,

$$\hat{\rho}_{\text{II}}(\hat{z}) = \hat{\rho}_{\text{II}}^{\text{lin}}(\hat{z}) + \frac{1}{\hat{\rho}_s} \int_0^{\infty} d\hat{z}_1 \hat{\rho}_{\text{II}}^2(\hat{z}_1) G_{\rho}^{\text{lin}}(\hat{z} - \hat{z}_1), \quad (8)$$

where  $G_{\rho}^{\text{lin}}(\hat{z}) = \hat{z} e^{-\hat{z}} \theta(\hat{z})$  (with  $\theta(x)$  denoting the Heaviside function) is the Green's function for the linear part of Eq. (4). Iteration of Eq. (8) yields  $\hat{\rho}_{\text{II}}(\hat{z})$  as a power series in  $\varepsilon$ . The result, together with  $\hat{\rho}_{\text{I}}(\hat{z})$  given by Eq. (3), can then be fed into Eq. (5) to give  $\hat{h}(\hat{z})$ .

We have carried out the above procedure to the first order in  $\varepsilon$ . Figure 2 shows typical  $\hat{h}$ - and  $\hat{\rho}$ -profiles as obtained from our zeroth order (thin solid lines) and first order (dashed lines) analytical solution for  $\hat{\rho}_s = 4$ . As anticipated earlier, the  $\hat{\rho}$ -profiles (black) for the motile population have the shape of a bulge with a depletion zone right ahead of the front at  $\hat{z} = 0$ . In the zeroth order approximation, the bulge is located at  $\hat{z} = 1$  with a peak value  $\hat{\rho}_m^{\text{lin}} = 2\hat{\rho}_c/e \simeq 0.736\hat{\rho}_c$ . For the values of  $\hat{D}_h$  and  $\hat{\beta}$  shown, the AHL profiles (red) also develop a dip in the contact zone. Nonetheless, the traveling wave solutions are self-consistent as  $\hat{h}$  never cross the threshold (dotted horizontal line) on the motile side.

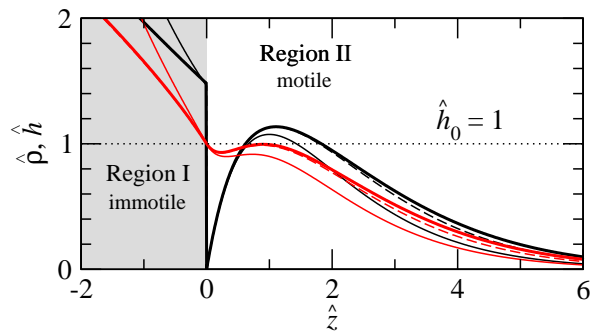


FIG. 2: (Color online.) Profiles of scaled cell density  $\hat{\rho}(\hat{z})$  (black) and AHL concentration  $\hat{h}(\hat{z})$  (red) around the edge of the advancing aggregate at  $\hat{z} = 0$ . Shown here are the analytical solution to the zeroth order (thin solid lines) and first order (dashed lines) in  $\varepsilon = \hat{\rho}_c / \hat{\rho}_s$ , and the numerically exact solution to the steady traveling-wave equations (thick solid lines). Here  $\hat{D}_h = D_h / D_\rho = 1$ ,  $\hat{\beta} = \beta / \gamma = 4$ , and  $\hat{\rho}_s = \alpha \rho_s / \beta h_0 = 4$ .

To test our analytical solution we have calculated the steady traveling profiles by integrating Eqs. (1)-(2) numerically in the moving frame for the above boundary conditions (thick solid lines). As is evident from Fig. 2, the zeroth order solution already captures the key features of the solution while the first order solution shows quantitatively excellent agreement even at  $\hat{\rho}_s = 4$ .

Given this good agreement, we can now use the analytical expressions to find the stability limit of the traveling wave solution, i.e., parameter values for which the peak height  $\hat{h}_m$  of  $\hat{h}_{\text{II}}(\hat{z})$  reaches the threshold value  $\hat{h}_0 = 1$ . Let us first consider  $\hat{D}_h = D_h / D_\rho \simeq 1$  as in the experiments. The Green's function (6) decays at a rate of order one in scaled units when the scaled AHL diffusion length  $\hat{L}_h = \sqrt{\hat{D}_h / \hat{\beta}} \sim 1 = \hat{L}_\rho$ , but much faster when  $\hat{L}_h \ll 1$ . In the latter case, the AHL profile follows closely the cell density profile, reaching its peak value at the tip of the bulge. A straightforward exercise based on Eq. (7) of the linear case shows  $\hat{h}_m = \hat{\rho}_m = 2\hat{\rho}_c/e$  while  $\hat{h}(0) = \hat{\rho}_c/2 = 1$ . Hence  $\hat{h}_m = 4/e \simeq 1.47 > \hat{h}_0$ . In this case the traveling wave solution is not self-consistent. An increase of  $\hat{L}_h$  allows immotile cells to contribute more to the AHL level in the motile region. Consequently  $\hat{h}_{\text{II}}(\hat{z})$  flattens while  $\hat{\rho}_c$  decreases at the same time. Eventually  $\hat{h}_m$  drops to a value below  $\hat{K}_h$  to restore self-consistency of the traveling wave solution.

The actual stability limit can be obtained by numerically solving the equations  $\hat{h}_{\text{II}}(\hat{z}_m) \equiv \hat{h}_m = 1$  and  $\partial_{\hat{z}} \hat{h}_{\text{II}}(\hat{z}_m) = 0$ , where  $\hat{z}_m$  is the peak position of the AHL profile. Using the respective analytical profiles, we obtain the zeroth order  $\hat{\beta} = \phi^{\text{lin}}(\hat{D}_h)$  (thin solid line) and first order  $\hat{\beta} = \phi^{(1)}(\hat{D}_h)$  (dashed line) phase boundaries as shown in Fig. 3. In the latter case, the first order AHL profile allows us to compute the shift  $\delta\hat{\beta} = -\varepsilon\psi(\hat{D}_h)\phi^{\text{lin}}(\hat{D}_h)$  in  $\hat{\beta}$  that satisfies these equations

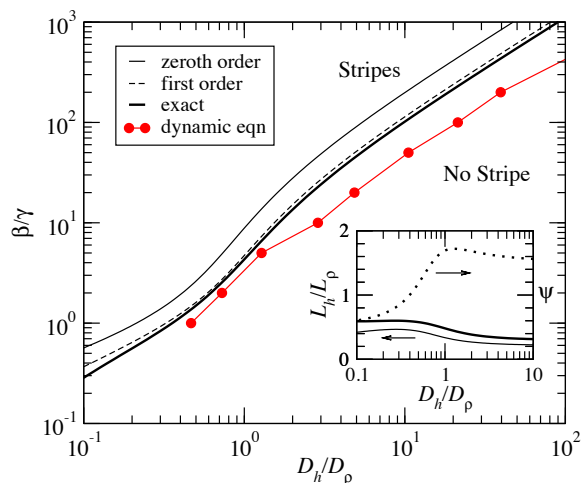


FIG. 3: Phase diagram for stripe formation. The thin solid and dashed curves are, respectively, the phase boundaries as calculated from our analytical solution in zeroth and first order in  $\varepsilon = \rho_c/\rho_s$ . The thick solid line is obtained from the numerical solution of Eqs. (1)-(2) in the moving frame. The red line represents the boundary determined from the onset of stripe patterns based on simulation of the full kinetic model (1)-(2). Inset: thin and thick solid lines give  $L_h/L_\rho$  on the zeroth order and exact phase boundaries, respectively. The dotted line shows the function  $\psi(D_h/D_\rho)$  from the first order correction in  $\varepsilon$  to the boundary position.

to order  $\varepsilon$  at a given  $\hat{D}_h$ . The modified boundary is then obtained from  $\phi^{(1)}(\hat{D}_h) = \phi^{\text{lin}}(\hat{D}_h) \exp[-\varepsilon\psi(\hat{D}_h)]$ . The function  $\psi(\hat{D}_h)$  is given by the dotted line in the inset of Fig. 3. As a comparison, we have also computed the phase boundary  $\hat{\beta} = \phi(\hat{D}_h)$  where  $\hat{h}_m = 1$  using the numerically exact traveling wave solution (thick solid line in Fig. 3). The agreement with the first order phase boundary  $\phi^{(1)}(\hat{D}_h)$  is very good.

As a confirmation that our ansatz indeed captures the dynamic instability behind the stripe formation process, we also show in Fig. 3 (red dots) the actual onset of stripes observed from a numerical simulation of Eqs. (1)-(2). Due to the time it takes for transient stripes to dissipate close to the transition with the setup of Fig. 1(b), the simulation tends to underestimate the no-stripe region. Thus the true phase boundary in the long-time limit is expected to be somewhat above the red line.

This study has led to the following picture of the stripe formation process: the growth and lateral expansion of the colony into an initially cell free region is described by a traveling wave solution. In the steadily propagating case, the density-coupled cell motility control breaks the colony into an immotile region behind a moving boundary and a density bulge of motile cells ahead of it. Maximum cell density in the motile region is reached at a distance  $L_\rho = \sqrt{D_\rho/\gamma}$  from the boundary. In the experiments of Ref. [15], the density coupling is implemented via a small molecule AHL which provides information on

cell density within a distance  $L_h = \sqrt{D_h/\beta}$ . We have shown that the steadily propagating wave is stable when  $L_h$  is greater than or comparable to  $L_\rho$ . In the opposite case  $L_h \ll L_\rho$ , instability develops as the maximum AHL concentration in the motile region would exceed the threshold  $h_0$  for motility suppression. Instead, the colony expands with periodic nucleation of new immotile regions within the motile bulge ahead of the previously formed high-density strip. Cell density behind the moving front continue to grow until nutrient exhaustion, where the density modulation becomes frozen. From the inset of Fig. 3 we see that the ratio  $L_h/L_\rho$  generally lies around 0.5 on the phase boundary between the two regimes.

In our system the propagating front thus drives sequential stripe formation in an open geometry. This is very different from the classical Swift-Hohenberg [19] mechanism where finite-wavelength symmetry breaking instability develops in the bulk. The highly nonlinear and localized process in the nucleation of new stripes also makes our mechanism different from that of pattern formation driven by fronts propagating into a bistable system where modulations arise during the linear instability development at the front [20]. In this respect, there are some similarities between our system and the nonperiodic Liesegang patterns since in both cases new “phase” precipitates when certain critical density is reached [21]. On the other hand, in the chemical systems that exhibit Liesegang patterns, reactant density increases via transport instead of growth.

We thank J. Tailleur and H. Levine for discussions. The work is supported in part by the Research Grants Council of the HKSAR under grants HKU1/CRF/10 (JDH) and 201910 (LHT).

- 
- [1] C.M. Chuong and M.K. Richardson, *Int. J. Dev. Biol.* **53**, 653 (2009).
  - [2] S. Kondo and T. Miura, *Science* **329**, 1616 (2010).
  - [3] E. Ben-Jacob, I. Cohen, and H. Levine, *Adv. Phys.* **49**, 395 (2000).
  - [4] E.O. Budrene and H.C. Berg, *Nature* **349**, 630 (1991).
  - [5] H. Fujikawa, *Physica A* **189**, 15 (1992).
  - [6] T. Matsuyama et al., *J. Bacteriol.* **182**, 385 (2000).
  - [7] T.J. Pedley and J.O. Kessler, *Ann. Rev. Fluid. Mech.* **24**, 313 (1992).
  - [8] R. Welch and D. Kaiser, *PNAS* **98**, 14907 (2001).
  - [9] E.F. Keller and L.A. Segel, *J. Theor. Biol.* **26**, 399 (1970).
  - [10] J. Murray, *Mathematical Biology* (Springer, Berlin, 1989).
  - [11] M.J. Schnitzer, *Phys. Rev. E* **48**, 2553 (1993).
  - [12] K. Kawasaki et al., *J. Theor. Biol.* **188**, 177 (1997).
  - [13] J. Tailleur and M.E. Cates, *Phys. Rev. Lett.* **100**, 218103 (2008).
  - [14] M.E. Cates et al., *PNAS* **107**, 11715 (2010).
  - [15] C. Liu et al., *Science* **334**, 238 (2011).
  - [16] H. C. Berg, *E. coli in Motion* (Springer, New York, 2004).
  - [17] R. McMurtrie, *Math. Biosc.* **39**, 11 (1978).

- [18] W. van Saarloos, Phys. Rev. A **37**, 211 (1988).
- [19] M.C. Cross and P.C. Hohenberg, Rev. Mod. Phys. **65**, 851 (1993).
- [20] G.T. Dee and W. van Saarloos, Phys. Rev. Lett. **60**, 2641 (1988).
- [21] M. Droz, J. Stat. Phys. **101**, 509 (2000).

## Supporting Material: Stripe formation in bacterial systems with density-dependent motility

As mentioned our model can be derived by coarse-graining of the microscopic dynamics. Generally, this procedure yields a mixture of two terms  $\partial_x(\mu(h)\partial_x\rho) + \theta\partial_x(\rho\partial_x\mu(h))$ , where  $\theta$  depends on the underlying microscopic dynamics, e.g.  $\theta = 1$  for Ito-dynamics and  $\theta = 1/2$  for Stratonovich dynamics [1]. With this general coupling our model becomes

$$\frac{\partial h}{\partial t} = D_h \frac{\partial^2 h}{\partial x^2} + \alpha\rho - \beta h, \quad (\text{S1})$$

$$\frac{\partial \rho}{\partial t} = \frac{\partial^2}{\partial x^2} (\mu(h)\rho) - (1 - \theta) \frac{\partial}{\partial x} \left( \rho \frac{\partial \mu(h)}{\partial x} \right) + \gamma_0 \rho \left( 1 - \frac{\rho}{\rho_s} \right). \quad (\text{S2})$$

In the main text, we study the case  $\theta = 1$ . In the following, we demonstrate that for  $\theta < 1$  the moving front still acts as an absorbing boundary and that our main conclusions remain valid in this case.

### Boundary conditions at the moving front $z = 0$ .

The field  $h(x)$  is continuous at  $h = K_h$  and even differentiable. This can be seen by integrating Eq. (S1) from  $z = 0^-$  to  $z = 0^+$  (as in the main text  $z = x - ct$ ) and by using  $\partial h/\partial t = -c\partial h/\partial z$ .

$$cw = -c[h(0^+) - h(0^-)] = D_h \partial h/\partial z|_{z=0^-}^{z=0^+}, \quad (\text{S3})$$

implying  $\partial h(z)/\partial z|_{0^+} = \partial h(z)/\partial z|_{0^-}$  as  $w \rightarrow 0$ .

In contrast, the density  $\rho(z)$  is discontinuous at  $z = 0$  with

$$\begin{aligned} \rho(0^+) - \rho(0^-) &= -\frac{1}{c} \frac{\partial(\mu(h)\rho)}{\partial z} \Big|_{z=0^-}^{z=0^+} + \frac{(1-\theta)\rho}{c} \frac{\partial(\mu(h))}{\partial z} \Big|_{z=0^-}^{z=0^+} = -\theta \frac{\rho}{c} \frac{\partial(\mu(h))}{\partial z} \Big|_{z=0^-}^{z=0^+} \\ &= -\theta \frac{D_\rho \rho(0^+)}{w} \frac{\partial h}{\partial z} \Big|_{z=0}, \end{aligned} \quad (\text{S4})$$

where we have used that  $\mu(h(z = 0^+)) = \mu(h(z = 0^-))$ . Eq. (S4) thus implies  $\rho(0^+) = 0$  as  $w \rightarrow 0$ . Thus, independent of the value of  $\theta$  the moving front acts as absorbing boundary. From this analysis it is also evident that the boundary condition  $\rho(0^+) = 0$  does not depend on our assumptions on the specific functional form of the interpolating function  $D_\rho(h)$  for  $K_h - w < h < K_h$ .

Finally, the slope of  $\rho(0^+)$  can be determined by integrating Eq. (S1) from  $z = 0^-$  to  $z = 0^+$

$$\partial \rho/\partial z|_{z=0^+} = c\rho_c/D_\rho, \quad (\text{S5})$$

where (as in the main text)  $\rho_c = \rho(0^-)$ .

**Results for  $\theta < 1$ .** We have calculated the cellular density profile and the phase diagram for different values  $\theta < 1$ . As can be seen from Fig. S1 the additional term in Eq. (S2) only leads to very small (hardly visible) modifications of the cellular density and AHL concentration profile. Consequently, the phase boundary is also not affected by the value of  $\theta$ .

---

[1] N.G. van Kampen, *Stochastic Processes in Physics and Chemistry* (Elsevier, Amsterdam, 2004).

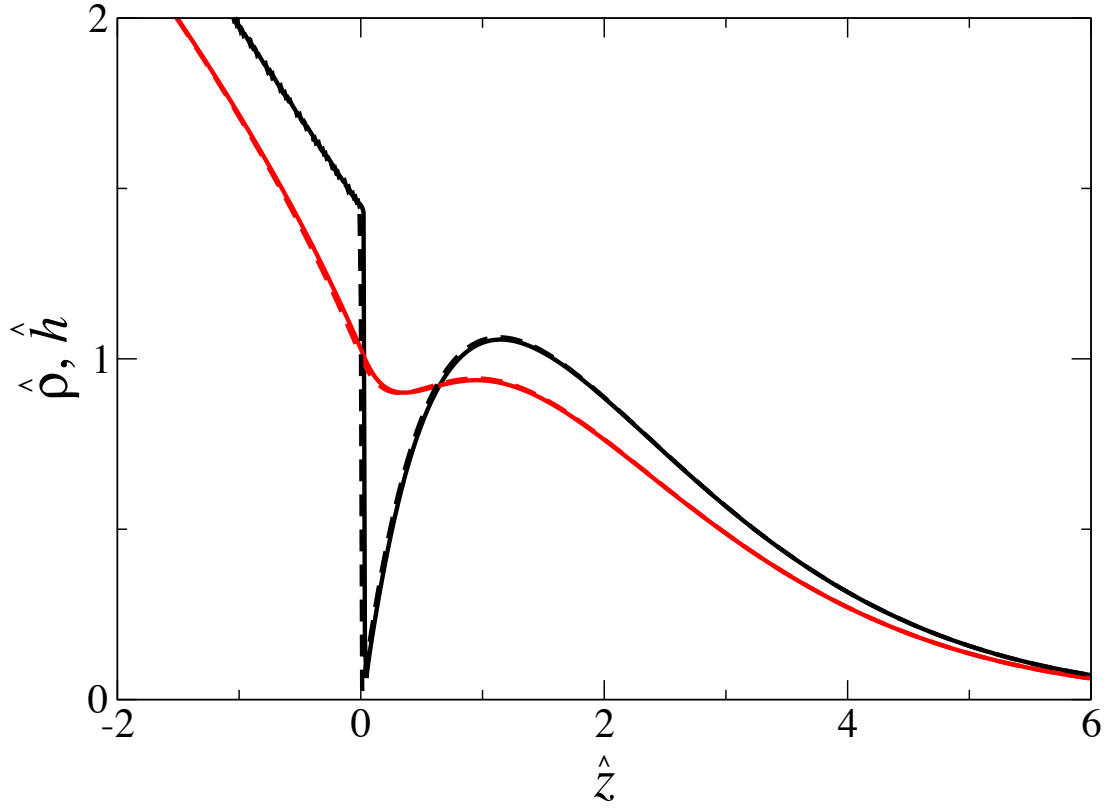


FIG. S1: Profiles of scaled cellular density  $\hat{\rho}(\hat{z})$  (black) and AHL concentration  $\hat{h}(\hat{z})$  (red) close to the moving front at  $\hat{z} = 0$  as calculated numerically from Eqs. (S1) and (S2). The solid lines are for  $\theta = 1/2$  the dashed lines for  $\theta = 1$ . Data are for  $\hat{D}_h = D_h/D_\rho = 1.3$ ,  $\hat{\beta} = \beta/\gamma = 5$ , and  $\hat{\rho}_s = \alpha\rho_s/\beta h_0 = 4$ .